Plasmonics
DOI 10.1007/s11468-009-9096-0

On the Surface Plasmon Resonance Modes of Metal Nanoparticle Chains and Arrays

Ergun Simsek

Received: 10 March 2009 / Accepted: 31 May 2009
© Springer Science + Business Media, LLC 2009

Abstract A method for estimating the surface plasmon resonance modes of metal nanoparticle chains and arrays within a multilayered medium is proposed. In this fully retarded point-dipole method, an inhomogeneous background is replaced with a homogeneous one, based on an effective refractive index approximation. The proposed method includes the effects of retardation, radiative damping, and dynamic depolarization due to the finite size of the nanoparticles. The use of diagonal terms of dyadic Green's functions and different polarizability coefficients along the semi-axes of ellipsoidal nanoparticles provides a complete set of both longitudinal and transverse resonance modes. Numerical results are compared with experimental results found in the literature.

Keywords Nanoparticle chains and arrays · Surface plasmon resonance modes · Multilayered background · Effective refractive index · Wavelength-dependent refractive index

Introduction

Surface plasmons (SPs) are of interest to a wide spectrum of engineers and scientists, due to their potential for developing new types of photonic devices and sensors. It has been shown, both theoretically and experimentally, that periodically located nanoparticles (NPs) can lead to giant electromagnetic field enhancement, which can be useful for detecting molecules at low concentrations [1–8]. Surface- [8–16] or tip- [17, 18] enhanced Raman scattering and nonlinear frequency generation [19] are some of the current SP applications. In these works, researchers tune up the properties of SPs and their interaction with light by changing the shape, size, and material composition of the NPs [1–26]. The purpose of this paper is to assist the design and analysis of such NP chains and arrays in the development of tools; specifically, the development of a method to estimate the wavelengths (or frequencies) for surface plasmon resonance (SPR) peaks occur for metal NP chains and arrays in multilayered structures.

In the last decade, many researchers have studied SPR modes of NP chains [7, 27–41] and arrays [3, 4, 41–49]. Some of these works deal with NPs fabricated on top of a glass slide, which can be viewed as the main component of transmission spectroscopy-based nanosensors. These researchers support their experimental results with finite difference time domain methods that can handle the inhomogeneous background [39, 41, 47, 48]. Some attempts to circumvent this inhomogeneity use index matching fluids [40], where the theoretical models based on the discrete dipole approximation (DDA) are used to calculate SPR modes of NP chains. Even though such efforts decrease the contrast between the surrounding media, the number of layers is generally more than two for many plasmonic structures. For example, coating the base structure with indium tin oxide (ITO) is a commonly used procedure to minimize the charging during fabrication and this procedure inevitably creates an additional layer. As such, if the background is a multilayered structure, DDA can be still helpful given that it is implemented via layered media Green's functions (LMGFs). However, the evaluation of these computationally intensive LMGFs is a bottleneck for many researchers due to their mathematical complexity. In [26, 40], researchers try to overcome this

E. Simsek (✉)
Department of Electrical and Electronics Engineering,
Bahcesehir University,
Ciragan C Osmanpasa Mektebi S. 4-6, Besiktas,
34100 Istanbul, Turkey
e-mail: ergun.simsek@bahcesehir.edu.tr

Published online: 09 June 2009

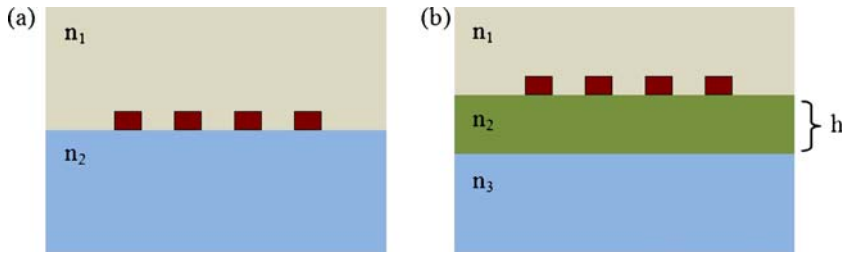

Fig. 1 **a** NPs in a two-layer medium and **b** NPs in a three-layer medium, where the height of the midlayer is *h*. *Maroon rectangles* represent the NPs

problem by utilizing the image theory (IT). Experimental results support the validity of the theoretical model [40] but it is still unclear how IT can be implemented for structures with more than two layers, especially for the case where the width of the layer (on which NPs are aligned) is less than the half of the height of the NPs.

To resolve the complexity of these problems, a simple effective refractive index (ERI) approximation is adopted to obtain the SPR modes of metal NP chains and arrays in multilayered structures. In this approximation, if we deal with a half-space problem, we simply take the average of refractive indices of two neighboring layers. If the number of layers is more than two, ERI depends on the ratio of the width of the midlayers to the wavelength. This approximation is first applied to the one-dimensional (1D) periodically located NP chains. Numerical results show that ERI provides very close results to the ones obtained experimentally. Then, similar to Auguié and Barnes [49], this approximation is applied to the two-dimensional (2D) periodically located NP arrays by extending the theory developed by Weber and Ford [37] for the 1D case. Different from [49], this work searches for SPR wavelengths (frequencies) on the complex frequency (ω) domain; hence, not only the resonant wavelengths can be revealed but also the propagation lengths. This fully retarded theoretical model includes the effects of retardation, radiative damping, and dynamic depolarization due to the finite size of the NPs based on the modified long-wavelength approximation (MLWA) [24]. In addition, the use of different polarizability coefficients along the semi-axes of ellipsoidal NPs reveals the existence of one longitudinal and two transverse resonance modes.

Effective index approximation and SPR modes of NP arrays

Crozier et al. study SPR modes of gold nanoparticle chains fabricated on ITO-coated glass slides both experimentally and numerically [39]. For the numerical analysis, they apply DDA technique twice to calculate SPR modes: In the first set, NPs are assumed to be in air; in the second set, NPs are assumed to be in a homogeneous glass medium. Interestingly, experimentally obtained dispersion results lay in between those two theoretical cases (see Fig. 4). Same research group studies the effect of ITO layer's thickness numerically in [41] and they conclude that 15 to 30 nm ITO layer causes a red shift in resonance frequencies. Inspired by these experimental studies, a simple ERI model is adopted for multilayered backgrounds in this work. This model replaces the multilayered background with a homogeneous medium with a refractive index of $n_{\text{effective}}$. The value of the effective refractive index depends on each layer's refractive indices and the wavelength of the incident wave as explained below.

Figure 1a depicts a two-layer medium: NPs are aligned on top of a substrate with a refractive index of n_2 and surrounded by another homogeneous medium with a refractive index of n_1. In this case, effective refractive index is simply the average of those two layers' refractive indices, $n_{\text{effective}} = (n_1 + n_2)/2$. If the number of layers is more than two, the effect of midlayers, which clearly depends on the wavelength, λ, should also be included. Figure 1b demonstrates a three-layer background, where h is the height of the midlayer. If h is much less than the wavelength, the electromagnetic field does not propagate long enough in the midlayer. Thus, the refractive index of the midlayer has only a small effect on the electromagnetic field propagation. However, if h is comparable to the wavelength, then the impact of the midlayer's refractive index is great. As a result of this wavelength-layer

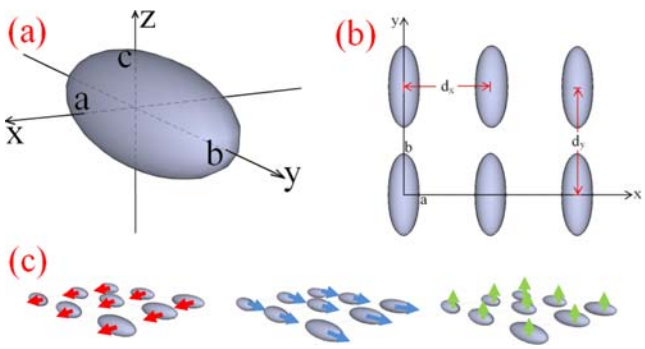

Fig. 2 **a** An ellipsoidal NP: semi-axes of the ellipsoids along the *x*-, *y*-, *z*-axes are *a*, *b*, and *c*. **b** Periodically located NP array on the *xy*-plane. Center-to-center distances along *x*- and *y*-axes are d_x and d_y, respectively. **c** Dipole moment orientations of metal NPs in longitudinal and transverse modes

Table 1 Polarizability coefficient calculation along the different axes of an ellipsoidal

Polarizability along the x-axis	Polarizability along the y-axis
$\alpha_{0,x} = \frac{\varepsilon_r-\varepsilon_b}{\varepsilon_b+L_x(\varepsilon_r-\varepsilon_b)}\frac{abc}{3}$	$\alpha_{0,y} = \frac{\varepsilon_r-\varepsilon_b}{\varepsilon_b+L_y(\varepsilon_r-\varepsilon_b)}\frac{abc}{3}$
$L_x = \frac{abc}{2}\int_{s=0}^{\infty}\left((s+a^2)^3(s+b^2)(s+c^2)\right)^{-1/2}ds$	$L_y = \frac{abc}{2}\int_{s=0}^{\infty}\left((s+a^2)(s+b^2)^3(s+c^2)\right)^{-1/2}ds$
$\alpha_x = \left(\frac{1}{\alpha_{0,x}} - i\frac{2}{3}k^3 - \frac{k^2}{a}\right)^{-1}$	$\alpha_y = \left(\frac{1}{\alpha_{0,y}} - i\frac{2}{3}k^3 - \frac{k^2}{b}\right)^{-1}$

thickness dependency, the following equation is used to calculate the ERI of a three-layer medium

$$n_{\text{effective}} = \begin{cases} \frac{1}{2}\left[n_1 + n_2\frac{h}{\lambda} + \left(1-\frac{h}{\lambda}\right)n_3\right], & (h \le \lambda), \\ \frac{n_1+n_2}{2}, & (h \ge \lambda). \end{cases} \quad (1)$$

Note that Eq. 1 simplifies into the two-layer case, when h is equal to zero. If the number of layers is more than three, a similar methodology can be followed.

ERI can easily be implemented in all DDA-based methods, including the ones proposed in [26, 31, 37, 38, 40]. Here, we follow the model developed by Weber and Ford [37]. The first example presented in the next section demonstrates the advantage of using ERI to obtain SPR modes of NP chains. To compute the SPR modes of NP arrays, we extend the model developed in [37] to 2D periodic structures as follows. Assume that there is an array ($N\times M$) of ellipsoidal metal NPs on the xy-plane. The semi-axes of the ellipsoids along the x-, y-, and z-axes are a, b, and c as shown in Fig. 2a. The interparticle spacing along x- and y-axes are d_x and d_y, respectively (see Fig. 2b), satisfying max(a, b, c) is less than min(d_x, d_y)/3. Two main components are required to calculate SPR modes: the polarizability factor and the dyadic Green's functions.

Since polarization vector is not uniform throughout the ellipsoids, different polarizability coefficients α_x, α_y, and α_z must be used along the x-, y-, and z-axes, respectively. As a result, there should be one longitudinal and two transverse SPR modes as depicted in Fig. 2c. The equations required for the calculation of the polarizability coefficients along the x- and y-axes are listed in Table 1. The relative permittivity values ε_r and ε_b stand for the metal NPs and the background, respectively, where $\varepsilon_b = n^2_{\text{effective}}$. The geometrical factor L_x or L_y defines relative polarizability along x- or y-axis, such that $L_x + L_y + L_z = 1$. The effects of retardation and depolarization are included based on MLWA [24]. Similar expressions exist for the nanoparticle polarizability along the z-axis, which are not shown here for the sake of brevity.

Dyadic Green's functions $G_{\xi\varphi}(R|R')$ give ξ-component of the electric field at R due to an oscillating point dipole located at R' directing φ-axis, where ξ and φ are either x, y, or z. For the problem of interest, only the diagonal terms of the dyadic Green's functions are needed. These terms can be written as

$$G_{xx}(\Delta x,\Delta y,\Delta z) = \left[\begin{matrix} -k^2\left(\Delta y^2+\Delta z^2\right) - (1+jkr) \\ \left(2-3\frac{\Delta y^2+\Delta z^2}{r^2}\right) \end{matrix}\right]\frac{e^{-jkr}}{r^3}, \quad (2a)$$

$$G_{yy}(\Delta x,\Delta y,\Delta z) = \left[\begin{matrix} -k^2\left(\Delta x^2+\Delta z^2\right) - (1+jkr) \\ \left(2-3\frac{\Delta x^2+\Delta z^2}{r^2}\right) \end{matrix}\right]\frac{e^{-jkr}}{r^3}, \quad (2b)$$

$$G_{zz}(\Delta x,\Delta y,\Delta z) = \left[\begin{matrix} -k^2\left(\Delta x^2+\Delta y^2\right) - (1+jkr) \\ \left(2-3\frac{\Delta x^2+\Delta y^2}{r^2}\right) \end{matrix}\right]\frac{e^{-jkr}}{r^3}, \quad (2c)$$

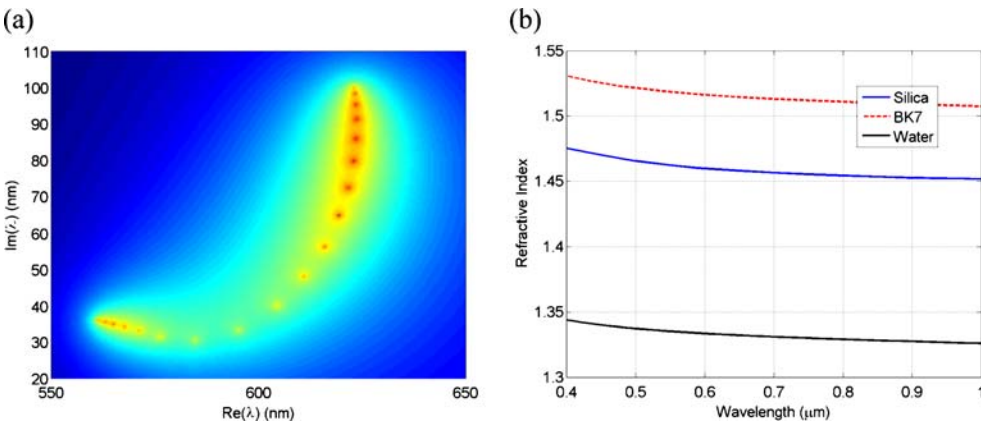

Fig. 3 **a** Determinant of **S** matrix for the longitudinal mode on the complex ω domain, where x- and y-axes are real and imaginary parts of ω: *red points* represent very low values, whereas *blues* depict the opposite. **b** Refractive indices of silica (*blue solid line*), borosilicate glass Schott BK7 (*red dashed line*), and water (*black solid line*) over a range of wavelengths

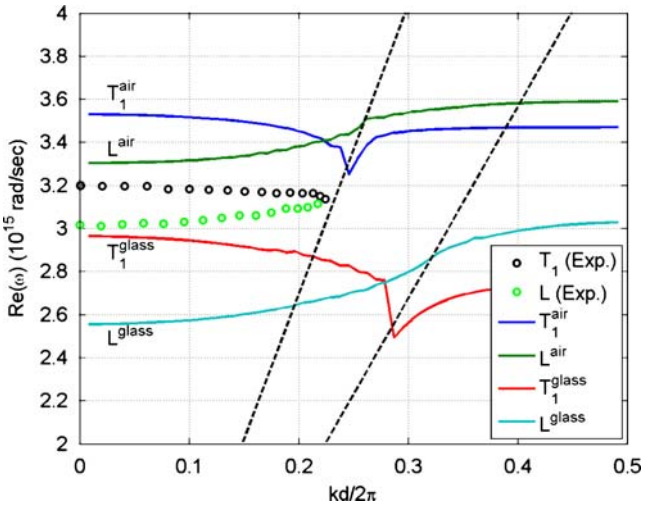

Fig. 4 SP dispersion relationship of metal nanoparticle chains: experiment (*dots*) vs. theory (*lines*). *Blue* and *green solid lines* depict theoretical T_1 and L results assuming background is air. *Red* and *magenta solid lines* depict theoretical T_1 and L results assuming background is glass. *Black solid* and *dashed lines* depict the light line in air and glass, respectively

where k is the wavenumber of the background medium, R and R' corresponds to x, y, and z and x', y', and z', respectively, in Cartesian coordinates; $\Delta x = x - x'$, $\Delta y = y - y'$, $\Delta z = z - z'$, and $r = (\Delta x^2 + \Delta y^2 + \Delta z^2)^{0.5}$. Note that Δz=0 for the problem of interest, but it would be nonzero for the structures with NPs at different heights.

SPR mode occurs when the dipole moment of a single oscillating particle becomes equal to the induced moment, which is defined by the sum of each surrounding particle's polarizability coefficient times the total electric field created by all the surrounding oscillating dipoles (Eqs. 3a–3c).

$$1 - \alpha_x \sum_{\text{all}} G_{xx}(x,y,z|x',y,z') = 0 \quad \text{Longitudinal mode (L)} \tag{3a}$$

$$1 - \alpha_y \sum_{\text{all}} G_{yy}(x,y,z|x',y,z') = 0 \quad \text{Transverse}-1\ \text{mode (T}_1\text{)} \tag{3b}$$

$$1 - \alpha_z \sum_{\text{all}} G_{zz}(x,y,z|x',y,z') = 0 \quad \text{Transverse}-2\ \text{mode (T}_2\text{)} \tag{3c}$$

For a finite number of particles, the above equations can be expressed in a matrix form similar to the 1D case [39] as follows:

$$\mathbf{S} = \begin{bmatrix} \psi & g_{1112} & g_{1113} & \cdots & g_{111N} & g_{1121} & \cdots & g_{11MN} \\ g_{1211} & \psi & g_{1213} & \cdots & g_{121N} & g_{1221} & \cdots & g_{12MN} \\ & & \ddots & & & & & \\ & & & \ddots & & & & \\ & & & & \ddots & & & \\ & & & & & \ddots & & \\ & & & & & & \ddots & \\ g_{MN11} & g_{MN12} & g_{MN13} & \cdots & g_{MN1N} & g_{MN21} & \cdots & \psi \end{bmatrix}_{MN\times MN}, \tag{4}$$

where $\psi = 1/\alpha_\gamma$ and $g_{ijkl} = -G_{\gamma\gamma}((i-j) \times d_x, (k-l) \times d_y, 0)$ and γ is x, y, or z. $\mathbf{S}$ is an $NM\times NM$ matrix and the

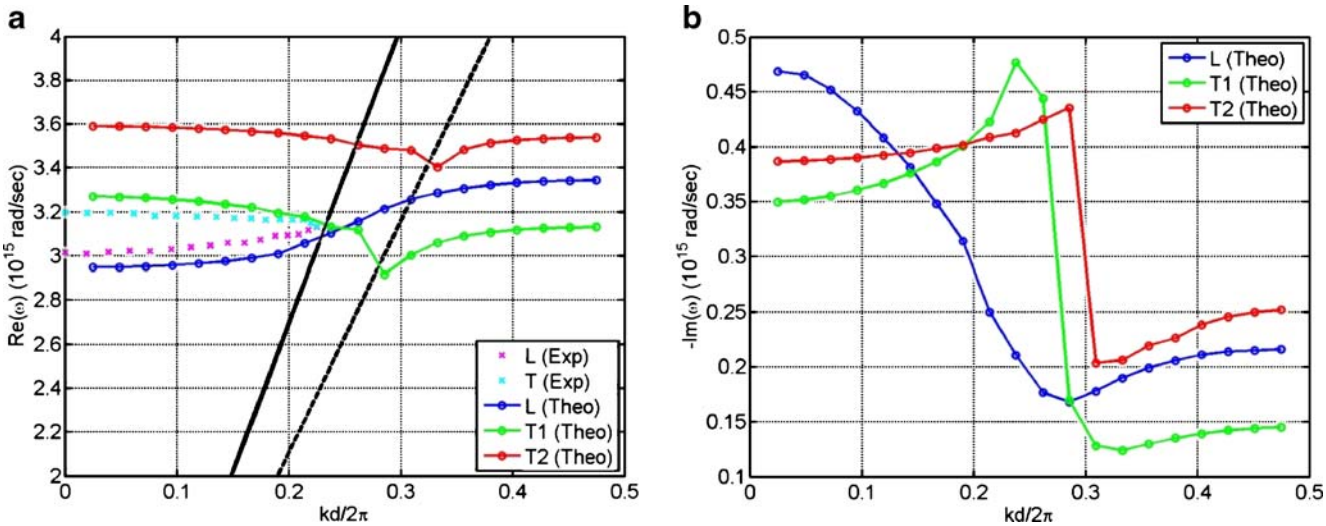

Fig. 5 **a** SP dispersion relationship of metal nanoparticle chains: experiment (*dots*) vs. theory (*lines*). *Black solid* and *dashed lines* depict the light line in air and effective medium, respectively. **b** Imaginary part of the resonant wavelengths in **a**

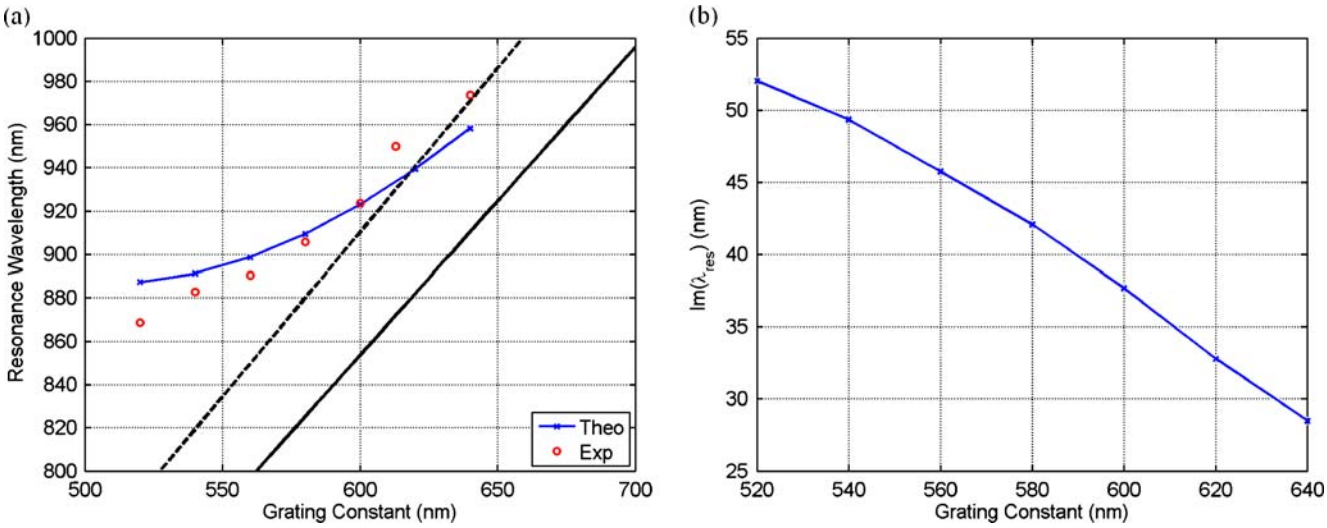

Fig. 6 **a** SPR modes of metal nanoparticle arrays: experiment (*red dots*) vs. theory (*blue line*) for $d_x=d_y$=520, 540, 560, 580, 600, 620, 640 nm. *Black dashed* and *solid lines* depict the first grating order in glass and effective medium, respectively. **b** The imaginary part of the resonant wavelengths in **a**

frequency values where the determinant of **S** is equal to zero define the SPR modes.

In order to find the complex zeros of determinant {**S**}, we calculate the determinant of **S** on a complex ω domain. Figure 3a is a typical output of this complex-root search (for the longitudinal mode of the NP chain explained in the first example of "Numerical results"). In this figure, *x*- and *y*-axes are real and imaginary parts of ω and each color represents the relative magnitude of the determinant$\{\mathbf{S}(\omega)\}$ at that particular ω value such that redness (blueness) indicates how small (large) the determinant$\{\mathbf{S}(\omega)\}$ is. In other words, red or yellow areas represent SPR modes where the real part of ω provides the resonant wavelength and the imaginary part provides insightful information about the propagation length [37, 38]. Once we roughly know where the resonant modes occur, we can zoom in and obtain these values more precisely.

The final detail of the numerical model is the refractive index of the substrate and water. Even though it has a small effect, for a more precise calculation of the SPR modes, a wavelength-dependent refractive index is implemented not only for metals but also for glasses and water. Figure 3b depicts refractive indices for silica [50], borosilicate glass Schott BK7 [51], and water [52] over a range of wavelengths.

Numerical results

Three different sets of experimental results found in the literature are compared with the proposed approach. For all examples, the experimental values for the optical constants of gold are used [53] rather than the Drude model, to avoid the concerns about the selection of the appropriate plasmon and relaxation frequency values. For the simulations, the number of NPs in the array is equal to 400 (20×20). The described algorithm is implemented using FORTRAN programming language with the quadruple precision.

One-dimensional chain of gold nanoparticles

In [39], gold NP chains are fabricated by e-beam lithography on ITO-coated glass slides. The gold disks are

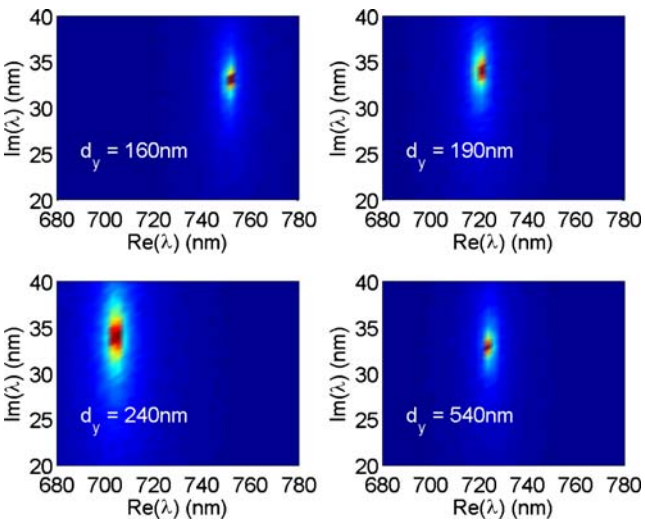

Fig. 7 The determinant of matrix **S** for 50-nm-height, 60-nm-wide, and 140-nm-long gold NP array with d_x=180 nm, d_y=160, 190, 240, or 540 nm. *x*- and *y*-axes are real and imaginary parts of λ and each color represents a determinant value such that the *red points* are very close to zero, whereas *blue parts* are much larger than zero. Note that in this configuration, there are two other SPR modes, L and T_2, at wavelengths shorter than 600 nm, which are not shown here for the sake of brevity

Table 2 SPR modes of metal nanoparticle arrays: experiment vs. theory

[a] d_x is fixed; d_y is varying for arrays of NPs of 50 nm height, 60 nm wide, and 140 nm long

[b] d_y is fixed; d_x is varying for arrays of NPs of 50 nm height, 40 nm wide, and 80 nm long

	d_x=180nm[a]			d_y=120nm[b]	
	$\lambda_{experiment}$	$\lambda_{theoretical}$		$\lambda_{experiment}$	$\lambda_{theoretical}$
d_y=160 nm	740	751+33.5i	d_x=60 nm	606	598+54.1i
d_y=190 nm	710	720+34.1i	d_x=90 nm	641	631+48.2i
d_y=240 nm	693	704+34.4i	d_x=140 nm	648	639+44.1i
d_y=540 nm	724	724+33.1i	d_x=240 nm	653	642+42.2i

92 nm in diameter and have a 55-nm thickness. The center-to-center distances are 140 nm along the length of the chain. The thickness of ITO coating is 20 nm. The refractive indices of ITO and air are assumed to be 1.45 and 1, respectively. In [39], Crozier et al. calculate two sets of dispersion relations. In the first set, NPs are assumed to be in the air. In the second set, the NPs are assumed to be in a homogeneous glass medium with a refractive index of 1.51. In Fig. , the experimental results [39] for the T_1 and L modes are plotted along with the calculated dispersion curves. Note that these curves are obtained with standard DDA (without ERI) and experimental results lay in between those two sets of theoretical results.

Figure 5a shows the same comparison as Fig. 4, but this time, DDA is implemented with the proposed effective refractive index approximation. Another difference of this approach is the use of wavelength-dependent refractive indices even for dielectrics: The glass is assumed to be a borosilicate glass Schott BK7 (n_{BK7} changes between 1.53 and 1.51, see Fig. 4). Numerical results do not perfectly agree with the experimental results—the maximum error is around 2.34%—but still provide much closer results than the numerical results depicted in Fig. 4 (which are the same as the ones in [39], where refractive index is either 1 or 1.51). When we compare Figs. 4 and 5, we can clearly observe the advantage of using effective refractive index approximation that deeply improves the accuracy of DDA.

In Fig. 5a, red line depicts the second-transverse mode (T_2) which fits well with the experimental results [39]. T_2 mode interacts strongly with the light line same as the T_1 mode. Figure 5b shows the imaginary part of resonance frequencies which can be used to estimate propagation lengths. It can be said that all modes generate strong far-field radiation above the light line.

Two-dimensional array of gold nanoparticles: d_x=d_y

In [48], Chu et al. study gold NP arrays fabricated on ITO-coated glass slides with interparticle spacing varying from 520 to 640 nm. The medium above the glass substrate is water. The radius and height of the cylindrical gold disks are 90 and 40 nm, respectively. The red points in Fig. 6a show resonance peak positions of the measured extinction cross section spectra as a function of grating constant. For the numerical simulation, a, b, and c values are assumed to be 90, 90, and 20 nm. The refractive index of water [52] changes between 1.3441 and 1.3260, and the glass is assumed to be a borosilicate glass Schott BK7. Blue solid line depicts the resonant modes obtained with 2D DDA method. Numerical results do not perfectly match to the experimental results but still provide a very good estimation: The maximum error is 2.25%. Figure 6b shows the imaginary part of the resonant wavelengths, which decreases almost linearly as grating constant increases. Since d_x=d_y and a=b, the longitudinal and the first transverse modes are equal to each other. The second transverse mode occurs at wavelengths shorter than 800 nm, so only the L and T_1 modes are seen in Fig. 6.

Two-dimensional array of gold nanoparticles: $d_x \neq d_y$

Smythe et al. present a systematic study of optical antenna arrays, in which gold nanorods are fabricated on 15-nm-thick ITO-coated silica substrates [47]. NPs are approximately 50 nm height, 60 nm wide, and 140 nm long. d_x is fixed to 180 nm while four different d_y values are experimented: 160, 190, 240, and 540 nm. The experimental study reveals that the first transverse resonance modes occur at 740, 710, 693, and 724 nm, respectively. In order to simulate this structure,

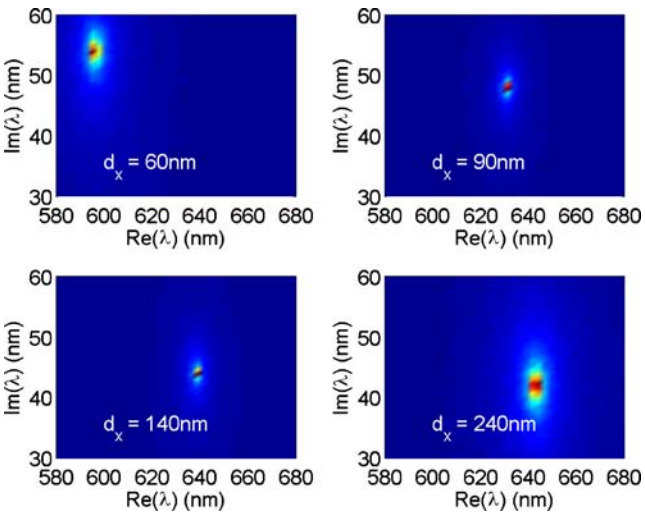

Fig. 8 Follows the Fig. 7 for 50-nm-height, 40-nm-wide, and 80-nm-long gold NP array with d_y=120 nm, d_x=60, 90, 140, or 240 nm

a wavelength-dependent refractive index is implemented for silica [50]. For the polarization vector, *a*, *b*, and *c* values are assumed to be 30, 70, and 25 nm, respectively. Figure 7 shows the magnitude of determinants for the first transverse mode. The complex λ value giving the smallest determinant corresponds to the resonance mode. Table 2 lists theoretically and experimentally found resonance wavelengths. Once again, the numerical approach provides a good estimate for the experiment: The maximum error is around 1.6%. From the numerical results, it can be observed that as d_y is increased from 160 to 240 nm, the resonance of the arrays blue-shifted from 751 to 704 nm and when d_y is further increased to 540 nm, the resonance underwent a red-shift, because of jumping to a higher grating order.

Similar procedure is followed for 50-nm-height, 80-nm-long, and 40-nm-wide nanorods. This time, d_y is fixed to 120 nm and d_x is varied from 60 to 90, 140, and 240 nm, step by step. The first transverse resonant modes occur at 606, 641, 648, and 653 nm, respectively. For the simulation, *a*, *b*, and *c* values are assumed to be 20, 40, and 25 nm, respectively. Figure 8 depicts the magnitude of the determinants for the first transverse mode. As summarized in Table 2, numerically obtained SPR wavelength values are very close to the experimental results: The maximum error between them is 1.69%. There are two other SPR modes, L and T_2, in this configuration as well. L mode occurs at wavelengths between 400 and 500 nm, whereas T_2 mode occurs between 500 and 600 nm.

All simulation results have discrepancies with the experimental results. The main reason behind these discrepancies is that the overall process is a series of assumptions and approximations. NPs, multilayered background, and circular cylinders are approximated by point dipoles, an effective medium, and ellipsoids, respectively. Moreover, the experimental factors, such as temperature, cause additional deviation between the experiment and this kind of DDA-based solutions. In order to calculate SPR modes precisely, a full-wave solver—either in time or frequency domain—should be used. Time domain solvers can handle inhomogeneous backgrounds, whereas frequency domain solvers should be implemented with layered medium Green's functions. In order to model materials as realistic as possible, temperature and wavelength-dependent refractive indices should be used. It should be also noted that the time and frequency domain full-wave solvers might have high memory and computation time requirements, unlike the DDA-based methods. If an improvement is required in the overall accuracy of DDA solution, one might consider following suggestions:

- Using layered medium Green's functions instead of ERI
- Following a numerical approach, such as [54], to calculate exact polarizability coefficients instead of approximate equations
- Using temperature and wavelength-dependent refractive index

Conclusions

A method for estimating the surface plasmon resonance modes of metal nanoparticle chains and arrays within a multilayered medium is proposed. This point-dipole method includes the effects of retardation, radiative damping, and dynamic depolarization due to the finite size of the nanoparticles. Numerical results show that point-dipole method implemented with the proposed effective refractive index approximation can provide a good estimate of the complete set of surface plasmon resonance modes in a multilayered medium, which might be very useful at the preexperimental stage.

References

1. Crozier KB, Sundaramurthy A, Kino GS, Quate CF (2003) Optical antennas: resonators for local field enhancement. J Appl Phys 94:4632–4642
2. Hao E, Schatz GC (2004) Electromagnetic fields around silver nanoparticles and dimmers. J Chem Phys 120:357–366
3. Genov DA, Sarychev AK, Shalaev VM, Wei A (2004) Resonant field enhancements from metal nanoparticle arrays. Nano Lett 4:153–158
4. Zou SL, Schatz GC (2005) Silver nanoparticle array structures that produce giant enhancements in electromagnetic fields. Chem Phys Lett 403:62–67
5. Sundaramurthy A, Crozier KB, Kino GS, Fromm DP, Schuck PJ, Moerner WE (2005) Field enhancement and gap-dependent resonance in a system of two opposing tip-to-tip Au nanotriangles. Phys Rev B 72:165409
6. Cubukcu E, Kort EA, Crozier KB, Capasso F (2006) Plasmonic laser antenna. Appl Phys Lett 89:093120
7. Guillon M (2006) Field enhancement in a chain of optically bound dipoles. Opt Express 14:3045–3055
8. Kneipp K, Wang Y, Kneipp H, Perelman LT, Itzkan I, Dasari RR, Feld MS (1997) Single molecule detection using surface-enhanced Raman scattering (SERS). Phys Rev Lett 78(9):1667–1670
9. Kneipp K, Kneipp H, Itzkan I, Dasari RR, Feld MS (2002) Surface-enhanced Raman scattering and biophysics. J Phys Condens Matter 14:R597–R624
10. Félidj N, Aubard J, Lévi G, Krenn JR, Salerno M, Schider G, Lamprecht B, Leitner A, Aussenegg FR (2002) Controlling the optical response of regular arrays of gold particles for surface-enhanced Raman scattering. Phys Rev B 65:075419
11. Félidj N, Lau Truong S, Aubard J, Lévi G, Krenn JR, Hohenau A, Leitner A, Aussenegg FR (2004) Gold particle interaction in regular arrays probed by surface enhanced Raman scattering. J Chem Phys 120:7141–7146
12. Grand J, Lamy M, de la Chapelle JL, Bijeon PM, Adam AV, Royer P (2005) Role of localized surface plasmons in surface-enhanced Raman scattering of shape-controlled metallic particles in regular arrays. Phys Rev B 72:033407
13. Laurent G, Félidj N, Aubard J, Lévi G, Krenn JR, Hohenau A, Schider G, Leitner A, Aussenegg FR (2005) Evidence of

multipolar excitations in surface enhanced Raman scattering. Phys Rev B 71:045430
14. Fromm DP, Sundaramurthy A, Kinkhabwala A, Schuck PJ, Kino GS, Moerner WE (2006) Exploring the chemical enhancement for surface-enhanced Raman scattering with Au bowtie nanoantennas. J Chem Phys 124:061101
15. Billot L, Lamy M, de la Chapelle AS, Grimault AV, Barchiesi D, Bijeon JL, Adam PM, Royer P (2006) Surface enhanced Raman scattering on gold nanowire arrays: evidence of strong multipolar surface plasmon resonance enhancement. Chem Phys Lett 422:303–307
16. Su KH, Durant S, Steele JM, Xiong Y, Sun C, Zhang X (2006) Wavelength-scanned surface-enhanced Raman excitation spectroscopy. J Phys Chem B 110:3964–3968
17. Stöckle RM, Suh YD, Deckert V, Zenobi R (2000) Nanoscale chemical analysis by tip-enhanced Raman spectroscopy. Chem Phys Lett 318:131–136
18. Pettinger B, Ren B, Picardi G, Schuster R, Ertl G (2004) Nanoscale probing of adsorbed species by tip-enhanced Raman spectroscopy. Phys Rev Lett 92:096101-1
19. Danckwerts M, Novotny L (2007) Optical frequency mixing at coupled gold nanoparticles. Phys Rev Lett 98:026104
20. Malinsky MD, Kelly KL, Schatz GC, Van Duyne RP (2001) Nanosphere lithography: effect of substrate on the localized surface plasmon resonance spectrum of silver nanoparticles. J Phys Chem B 105:2343–2350
21. Su KH, Wei QH, Zhang X, Mock JJ, Smith DR, Schultz S (2003) Interparticle coupling effects on plasmon resonances of nanogold particles. Nano Lett 3:1087–1090
22. Schider G, Krenn JR, Hohenau A, Ditlbacher H, Leitner A, Aussenegg FR, Schaich WL, Puscasu I, Monacelli B, Boreman G (2003) Plasmon dispersion relation of Au and Ag nanowires. Phys Rev B 68:155427
23. Rechberger W, Hohenau A, Leitner A, Krenn JR, Lamprecht B, Aussenegg FR (2003) Optical properties of two interacting gold nanoparticles. Opt Commun 220:137–141
24. Kelly KL, Coronado E, Zhao LL, Schatz GC (2003) The optical properties of metal nanoparticles: the influence of the size, shape and dielectric environment. J Phys Chem B 107:668–677
25. Sherry LJ, Jin R, Mirkin CA, Schatz GC, Van Duyne RP (2006) Localized surface plasmon resonance spectroscopy of single silver triangular nanoprisms. Nano Lett 6:2060–2065
26. Noguez C (2007) Surface plasmons on metal nanoparticles: the influence of shape and physical environment. J Phys Chem C 111:3806–3819
27. Markel VA (1993) Coupled-dipole approach to scattering of light from a one-dimensional periodic dipole structure. J Mod Opt 40:2281–2291
28. Takahara J, Yamagishi S, Taki H, Morimoto A, Kobayashi T (1997) Guiding of a one-dimensional optical beam with nanometer diameter. Opt Lett 22:475–477
29. Quinten M, Leitner A, Krenn JR, Aussenegg FR (1998) Electromagnetic energy transport via linear chains of silver nanoparticles. Opt Lett 23:1331–1333
30. Maier SA, Kik PG, Atwater HA (2002) Observation of coupled plasmon-polariton modes in Au nanoparticle chain waveguides of different lengths: estimation of waveguide loss. Appl Phys Lett 81:1714–1716
31. Maier SA, Brongersma ML, Kik PG, Atwater HA (2002) Observation of near-field coupling in metal nanoparticle chains using far-field polarization spectroscopy. Phys Rev B 65:193408
32. Li K, Stockman MI, Bergman DJ (2003) Self-similar chain of metal nanospheres as an efficient nanolens. Phys Rev Lett 91:227402
33. Quidant R, Girard C, Weeber JC, Dereux A (2004) Tailoring the transmittance of integrated optical waveguides with short metallic nanoparticle chains. Phys Rev B 69:085407
34. Wei QH, Su KH, Durant S, Zhang X (2004) Plasmon resonance of finite one-dimensional Au nanoparticle chains. Nano Lett 4:1067–1071
35. Simovski CR, Viitanen AJ, Tretyakov SA (2005) Resonator mode in chains of silver spheres and its possible application. Phys Rev E 72:066606
36. Park SY, Stroud D (2004) Surface-plasmon dispersion relations in chains of metallic nanoparticles: an exact quasistatic calculation. Phys Rev B 69:125418
37. Weber WH, Ford GW (2004) Propagation of optical excitations by dipolar interactions in metal nanoparticle chains. Phys Rev B 70:125429
38. Koenderink AF, Polman A (2006) Complex response and polariton-like dispersion splitting in periodic metal nanoparticle chains. Phys Rev B 74:033402
39. Crozier K, Togan E, Simsek E, Yang T (2007) Experimental measurement of the dispersion relations of the surface plasmon modes of metal nanoparticle chains. Opt Express 15:17482–17493
40. Koenderink F, de Waele R, Prangsma JC, Polman A (2007) Experimental evidence for large dynamic effects on the plasmon dispersion of sub-wavelength metal nanoparticle waveguides. Phys Rev B 76:201403 Rapid Communication
41. Yang T, Crozier KB (2008) Dispersion and extinction of surface plasmons in an array of gold nanoparticle chains: influence of the air/glass interface. Opt Express 16:8570
42. Brongersma ML, Hartman JW, Atwater HA (2000) Electromagnetic energy transfer and switching in nanoparticle chain arrays below the diffraction limit. Phys Rev B 62:R16356–R16359
43. Lamprecht B, Schider G, Lechner RT, Ditlbacher H, Krenn JR, Leitner A, Aussenegg FR (2000) Metal nanoparticle gratings: influence of dipolar particle interaction on the plasmon resonance. Phys Rev Lett 84(20):4721–4724
44. Haynes CL, McFarland AD, Zhao L, Van Duyne RP, Schatz GC, Gunnarsson L, Prikulis J, Kasemo B, Käll M (2003) Nanoparticle optics: the importance of radiative dipole coupling in two-dimensional nanoparticle arrays. J Phys Chem B 107:7337–7342
45. Burin AL, Cao H, Schatz GC, Ratner MA (2004) High-quality optical modes in low-dimensional arrays of nanoparticles: application to random lasers. J Opt Soc Am B 21:121–131
46. Zou S, Schatz GC (2004) Narrow plasmonic/photonic extinction and scattering lineshapes for one and two dimensional silver nanoparticle arrays. J Chem Phys 121:12606–12612
47. Smythe EJ, Cubukcu E, Capasso F (2007) Optical properties of surface plasmon resonances of coupled metallic nanorods. Opt Express 15(12):7439–7447
48. Chu Y, Schonbrun E, Yang T, Crozier KB (2008) Experimental observation of narrow surface plasmon resonances in gold nanoparticle arrays. Appl Phys Lett 93:181108–181111
49. Auguié B, Barnes WL (2008) Collective resonances in gold nanoparticle arrays. Phys Rev Lett 101:143902
50. Medhat M, El-Zaiat SY, Radi A, Omar MF (2002) Application of fringes of equal chromatic order for investigating the effect of temperature on optical parameters of a GRIN optical fibre. J Opt A Pure Appl Opt 4:174–179
51. Schott Glass Technologies (1992) Schott Optical Glass Catalog. Schott Glass Technologies, Duryen, PA Available at http://www.us.schott.com/advanced_optics/english/download/catalogs.html
52. Harvey AH, Gallagher JS, Levelt Sengers JMH (1998) Revised formulation for the refractive index of water and steam as a function of wavelength, temperature and density. J Phys Chem Ref Data 27:761
53. Rakic D, Djurisic AB, Elazar JM, Majewski ML (1998) Optical properties of metallic films for vertical-cavity optoelectronic devices. Appl Opt 37:5271–5283
54. Sihvola A, Venermo J, Yla-Oijala P (2004) Dielectric response of matter with cubic, circular-cylinder, and spherical microstructure. Microw Opt Technol Lett 41(4):245–248